ORIGINAL PAPER

Molecular simulations of adsorption of RDX and TATP on IRMOF-1(Be)

Andrea Michalkova Scott · Tetyana Petrova ·
Khorgolkhuu Odbadrakh · Donald M. Nicholson ·
Miguel Fuentes-Cabrera · James P. Lewis ·
Frances C. Hill · Jerzy Leszczynski

Abstract The influence of different sorption sites of isoreticular metal-organic frameworks (IRMOFs) on interactions with explosive molecules is investigated. Different connector effects are taken into account by choosing IRMOF-1(Be) (IRMOF-1 with Zn replaced by Be), and two high explosive molecules: 1,3,5-trinitro-s-triazine (RDX) and triacetone triperoxide (TATP). The key interaction features (structural, electronic and energetic) of selected contaminants were analyzed by means of density functional calculations. The interaction of RDX and TATP with different IRMOF-1(Be) fragments is studied. The results show that physisorption is favored and occurs due to hydrogen bonding, which involves the C-H groups of both molecules and the carbonyl oxygen atoms of IRMOF-1(Be). Additional stabilization of RDX and TATP arises from weak electrostatic interactions. Interaction with IRMOF-1(Be) fragments leads to polarization of the target molecules. Of the molecular configurations we have studied, the Be-O-C cluster connected with six benzene linkers (1,4-benzenedicarboxylate, BDC), possesses the highest binding energy for the studied explosives (-16.4 kcal mol^{-1} for RDX and -12.9 kcal mol^{-1} for TATP). The main difference was discovered to be in the preferable adsorption site for adsorbates (RDX above the small and TATP placed above the big cage). Based on these results, IRMOF-1 can be suggested as an effective material for storage and also for separation of similar explosives. Hydration destabilizes most of the studied adsorption systems by 1-3 kcal mol^{-1} but it leads to the same trend in the binding strength as found for the non-hydrated complexes.

Keywords Adsorption · B97-D · IRMOF-1 · RDX · TATP

A. M. Scott (✉) · F. C. Hill
U.S. Army Engineer Research and Development Center (ERDC),
Vicksburg, MS 39180, USA
e-mail: andrea@icnanotox.org

A. M. Scott · T. Petrova · J. Leszczynski
Interdisciplinary Nanotoxicity Center, Department of Chemistry,
Jackson State University,
Jackson, MS 39217, USA

K. Odbadrakh
Materials Science and Technology Division,
Oak Ridge National Laboratory (ORNL),
Oak Ridge, TN 37831, USA

D. M. Nicholson · M. Fuentes-Cabrera
Center for Nanophase Materials Sciences, and Computer Sciences
and Mathematics Division, Oak Ridge National Laboratory,
Oak Ridge, TN 37831, USA

J. P. Lewis
Department of Physics and Astronomy, West Virginia University,
Morgantown, WV 26506, USA

Introduction

Most conventional explosives contain nitro groups, however some novel explosives do not contain nitrogen at all; rather, they are based on organic peroxides. The most common of these peroxide-based explosive compounds is TATP (triacetone triperoxide or 1,1,4,4,7,7-hexamethyl-1,4,7-cyclononanatriperoxane; also called peroxyacetone; illustrated in Fig. 1a). TATP is one of the most sensitive explosives known, being extremely sensitive to impact, temperature change and friction. Acetone peroxide was the explosive used in the July 2005 London bombings [1]. TATP with multiple peroxide functionality is better oxygen-balanced than most commercial peroxides. Because of extreme sensitivity to shock and overall exothermic decomposition, it requires special precautions when handled [2, 3]. Despite these limitations, recently it has found use as an improvised
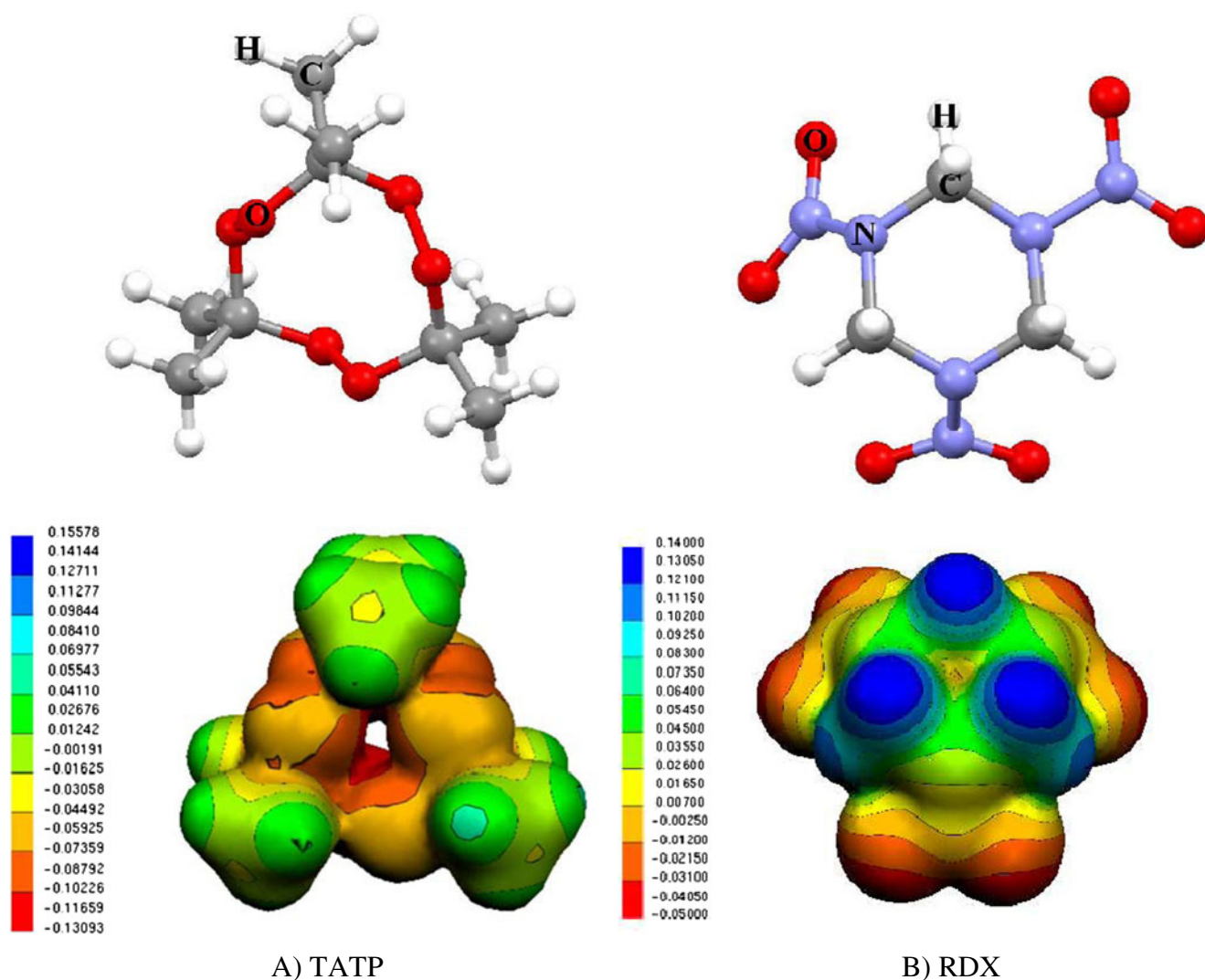
Fig. 1 The structure of isolated TATP (**A**), RDX (**B**) (legend: C-dark grey, H-white, O-red, N-dark blue) and their maps of electrostatic potential

explosive, because its synthesis is straightforward and requires only readily obtainable materials [4, 5].

1,3,5-Trinitro-s-triazine, also known as cyclotrimethylene trinitramine and RDX (displayed in Fig. 1b), is a secondary explosive. It has been the subject of a large number of studies regarding the sensitivity of energetic materials and the mechanisms of its decomposition [6]. The chair triaxial (AAA) form and chair diaxial (AAE) form are two of the most stable conformers of RDX [7–10]. The AAA conformer of RDX was chosen for this study since experimental infrared spectra of RDX vapor correlate well with simulated spectra of this RDX form, indicating that it may be the best structural representative of gaseous RDX [10].

Isoreticular metal-organic frameworks (IRMOFs) are a recently discovered class of nanoporous coordination polymers that are attracting considerable attention because of their extremely high surface areas (up to 4500 m^2/g) [11] and interchangeable organic linkers that enable relatively facile

manipulation of pore size and surface area through judicious ligand selection [12]. Recently, it has also been shown that both the size and chemical functionality of the MOFs pores can be systematically engineered to augment their surface area.

The flexibility, with which these components can be varied, has led to an extensive class of MOF structures with ultrahigh surface areas. In this paper we focus on IRMOF-1, which exhibits high thermal stability with decomposition occurring between 350 and 400°C [12]. IRMOF-1 (the most stable and the most porous among the MOF series [13]) has been frequently considered as a potential commercialized target for use in separation, catalysis, nonlinear optics, and storage of gases [13, 14]. IRMOF-1 was chosen because it represents a reference model phase that can be studied with *ab initio* methods at reasonable computational costs as has been confirmed by several computational studies [15, 16]. The structure of IRMOF-1 (shown in Fig. 2) consists of octahedral Be-O-C clusters (connectors, denoted as CON in

Fig. 2 The structure of used isolated IRMOF-1(Be) model that consists of one connector (denoted as CON) and six linkers (denoted as LIN, legend: C-dark grey, H-white, O-red, Be-blue). The position of big cage (denoted b) (A) and small cage (denoted s) (B) is shown
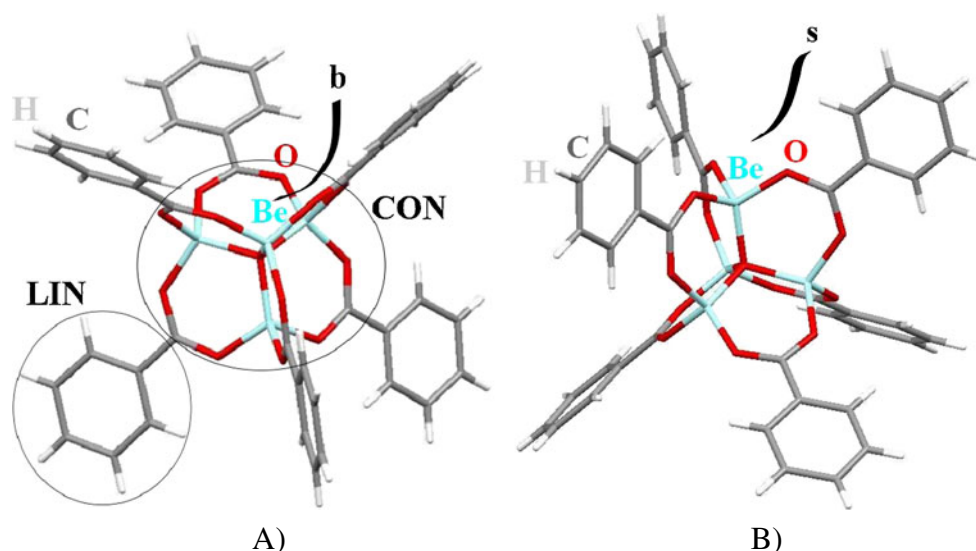
Fig. 2a) joined together by benzene linkers (denoted as LIN in Fig. 2a) to build a cubic three-dimensional framework that possesses a highly porous structure [17–19] (more detail explanation of the IRMOF-1 structure and models used in this study appears in Computational details section).

It is surprising that despite a significant interest in IRMOFs, only very few papers have been published that study these materials containing metals different than the original zinc. The possibility of tailoring the electronic properties and structure of M-IRMOF-1 (where M=Be, Mg, Ca, Zn, and Cd) by replacing the metal atom and by doping was investigated using density-functional theory (DFT) and a plane wave basis set [20]. Exchanging zinc with light main-group metals such as beryllium and magnesium was predicted to increase gas storage capacity, and exchange with transition metals could produce specific catalytic and magnetic properties [21]. Therefore, in this study we examined how substitution of zinc by beryllium in the connector can alter the sorption properties of IRMOF-1.

Since the adsorption of hydrogen in IRMOF-1 has been widely investigated at the DFT level and by using molecular mechanics simulations we will mention at least a few of these studies [22–28]. Microscopically, hydrogen interacts with the MOF via three principle attractive potential energy contributions: Van der Waals, charge-quadrupole, and induction [23, 25]. Metal-oxygen clusters are preferential adsorption sites for hydrogen in MOFs, and the effect of the organic linkers becomes evident with increasing pressure [24]. Monte Carlo (MC) simulations have identified strong binding sites at the connectors that became quickly saturated with 1.27 H_2 molecules at 78 K. At 300 K, a broad range of binding sites is observed [22]. It was also concluded that doping MOF with electropositive metals like lithium is a promising strategy for practical hydrogen storage [26].

Several experimental and theoretical papers (using molecular dynamics (MD)) were published on the adsorption and separation of natural gases and benzene in IRMOF-1 [29–34]. The simulations show that CO_2 is preferentially adsorbed over propane, ethane, methane and N_2 in the complete pressure range [29]. For argon and nitrogen molecules, the preferred adsorption site is near the zinc–oxygen cluster in the cavities where the linkers point outward [30]. MOF-5 represents a very open pore structure with liquid-like mobilities for benzene [31]. The experiments demonstrated that exchange of xenon from adsorption sites within the IRMOF to the free gas space is much slower than that between adsorption sites within the lattice [32].

Only a few computational studies related to MOFs in the presence of explosive compounds have been published [35–39]. MC simulations were used to generate adsorption isotherms for pure RDX, RDX in dry air, and RDX in wet air and provide adsorption energies and density distributions of the adsorbates within MOF [35]. The energy of adsorption of RDX at infinite dilution is -9.2 kcal mol⁻¹. Adsorption of RDX on IRMOF-1 is susceptible to changes in temperature [36]. The simulations at T=300 K suggest trapping configuration for RDX inside IRMOF-1 through H-bonding with three surrounding linkers. Different charge distributions were evaluated by comparing the binding energies from the classical potential (MD simulations and grand canonical Monte Carlo (GCMC)) with those from the quantum mechanical (QM) calculations for RDX adsorbed on IRMOF-10 [37]. The charge distribution was calculated so that the point charges were placed on the atom centers. Five different approaches, including the electrostatic potential method, Mulliken population analysis, Löwdin population analysis, natural bond orbital analysis and charges from the MM3 potential were used to assign point charges to IRMOF-10 structures obtained from QM calculations. Classical GCMC

and MD simulations of RDX in IRMOF-10 were performed using 15 combinations of charge sources of RDX and IRMOF-10. MC and MD simulations of RDX in IRMOF-10 show that as the charge distributions vary, the predicted interaction potential energies, the adsorption loading and the self-diffusivities are significantly different. The cage size and location of amine groups also affect the loading of RDX in different IRMOFs [38]. MD simulations at room temperature result in trapping configurations preferring TATP inside the IRMOF-8 cage, which could be attributed to molecular sieving effects [39].

Theoretical study of conformation and interactions between TATP and ions: Li^+, Cu^+, Zn^{2+}, Cd^{2+}, In^{3+}, Sb^{3+}, Sc^{3+}, and Ti^{4+} has shown that the bonds formed between TATP and Zn^{2+} and In^{3+} are the strongest [40]. A fast and simple electrochemical method for sensing peroxide-based explosives based on their acid treatment has been reported [41]. Also, a review of new analytical methods to determine peroxide-based explosives (for example TATP) in solid samples and air samples has been published [42]. The calculations of adsorption of TATP on hair surfaces suggest that the binding of explosive molecules to the lipid layer consists of interplay between dispersive and Coulomb interactions as well as the distortion of the lipid layer induced by the molecular adsorption. The relative importance of these effects depends on the chemical nature, the size, and the shape of the adsorbed molecule [43].

Preliminary investigations (performed only as a first approximation) focused on the interactions of RDX and TATP with small IRMOF-1(Zn) fragments [44]. It was shown that the selected explosive molecules interact more strongly with the linker of IRMOF-1(Zn) than with the connector. Hydrogen bonds and electrostatic interactions play a key role in the intermolecular interactions between IRMOF-1(Zn) and studied organic compounds. Due to very small models used and different level of theory applied, comparison with the results of this study is limited.

Our research seeks to utilize DFT-based approaches to shed light on the interactions of RDX and TATP with IRMOF-1 fragments with an emphasis on reactivity differences associated with the presence of water and the difference in the central cation of the IRMOF-1 connector. We believe that the insight gained through analysis of the RDX and TATP interactions with IRMOF-1 fragments can be applied to better understand the adsorption of these and other explosives on IRMOFs and to predict the preconcentrating of such contaminants so that they can be detected.

We would like to highlight that the results presented in this paper represent a comprehensive study, which considers different IRMOF-1(Be) models calculated at a level of theory (shown to be very efficient for the non-covalent interactions) with inclusion of dispersion forces. Many distinct interactions of RDX and TATP with the IRMOF-1(Be)

fragments were tested and different adsorption sites of this material were calculated and evaluated. Moreover, the influence of hydration on binding of the target molecule was also investigated. Understanding the interaction with water is of particular importance since the MOF crystal morphology is affected by exposure to water [45] and IRMOFs are water sensitive [13, 46]. This work also includes a detailed description of binding strength and polarization of the selected explosives adsorbed on IRMOF-1(Be), comparison with the results obtained for the interactions with IRMOFs(Zn) and extrapolation toward the storage and selection efficiency of IRMOF-1.

Simulation models and methods

All computations were performed within the Gaussian 09 program package [47] applying the DFT [48] B97-D functional. The B97-D method of Grimme [49] with empirical dispersion functions has been shown to work reasonably well for systems with weak intermolecular interactions. It is known that the B3LYP functional may lead to underestimation in the calculation of the interaction energy. An improved interaction energy can be obtained by the inclusion of an empirical interaction potential, such as is used in B97-D. The standard 6-31G(d) basis set was implemented.

Special attention was paid to the preparation of the IRMOF-1(Be) model, which was constructed to meet two main conditions. First, it needs to possess the proper elemental composition to treat interactions accurately with the target molecules and to minimize the cutoff effect (missing interactions with the bulk). Secondly, it should be a relatively small model (computationally inexpensive) if one aims to test various positions and orientations of adsorbate and calculate different properties of such systems in a reasonable time. Therefore, models were prepared to capture the site of IRMOF-1(Be) mainly responsible for the interactions with RDX and TATP as accurately as possible (identified from the results of previously published computational studies of variety of IRMOFs systems [35–39]).

The crystal structure of IRMOF-1 [12] was used as a starting point to prepare representative cluster models of this species. The models were constructed so that they contain one connector (C is used to denote the models in the text, Tables and Figure captions), site of IRMOF-1 (it consists of the Be_4O tetrahedron connected with the CO_2 groups $((Be_4O)(CO_2)_6)$ bounded with six linkers that possesses a C_6H_5 stoichiometry (notation L6 is used to denote the models in the text, Tables and Figure captions). The geometry of used IRMOF-1(Be) models (having one connector and six linkers (CL6)) is illustrated in Fig. 2a where the connector part is identified by a circle denoted CON and linker part is identified

by a circle denoted LIN. Due to the planarity of the linkers, the unit cell is formed by two different active cages [31], which are displayed separately in Figs. 2a and b. The slightly bigger cage shown in Fig. 2a (denoted b in the text, Figures and Tables) is characterized by the planes of the linker's perpendicular to a vector oriented toward the cell center. In the case of the small cage, displayed in Fig. 2b (denoted s in the text, Figures and Tables), the benzene rings point toward the cell center. The adsorption of RDX and TATP above both cages was calculated. All studied systems were electroneutral. In the text, figure captions and tables, the calculated systems will be denoted as CL6(s) and CL6(b), based on which cage is dominant.

It should be mentioned that although applied IRMOF-1 (Be) clusters are quite small, they could represent simple models of an IRMOF-1 surface. Similar methods and models were used to develop a new valence force field for MOF-5 [15] and to study the adsorption of hydrogen on MOF-5 [22, 23]. Similar size MOF models, applied in several theoretical studies of RDX and TATP interactions with a variety of IRMOFs [36–39], were found to accurately describe the studied interactions. Also, even smaller models of zeolites (to which the MOF systems are often compared, especially when dealing with the adsorption properties) used recently to calculate the adsorption of CO to gallium ions [50], adsorption of pyridine [51, 52] and adsorption of CH_3SH on their acidic sites [53], were concluded to be effective to obtain the binding energy of studied systems. Moreover, the same modeling technique was implemented previously to calculate the adsorption of explosive compounds on layered aluminosilicates characterized by a large interlayer space [54–57]. Therefore, within the accuracy of the applied computational method the system consisting of a target molecule and the IRMOF-1 fragments employed can be considered to simulate RDX or TATP adsorption.

The interaction energy (Eint) between a M ad-molecule (RDX, TATP) and an IRMOF fragment site (F) within a M-F complex (RDX-MOF or TATP-MOF) was obtained by calculating the total energies of the three systems involved and taking the difference according to expression (difference between the total energy of the RDX-, and TATP-MOF complex (M-F), and total energies of the subsystems (the RDX or TATP molecule (M) and the IRMOF-1(Be) fragment (F)):

$$Eint = E(M - F) - E(M) - E(F) \qquad (1)$$

The interaction energies were corrected for basis superposition error (BSSE, Ese) [58, 59] by the counterpoise (CP) method proposed by Boys and Bernardi [60] using the "ghost" atoms to obtain a counterpoise corrected interaction energy (Ecorr). This correction is needed due to the fact that the basis sets are not the same for different calculations. The size of basis set is larger for the complete system, implying

more degrees of freedom in the variational determination of the energy and leading to an unphysical energy lowering. In the CP method all basis functions of the other subsystem are added to the basis set of each subsystem without its electrons and nuclei (ghost functions). Then Ecorr is calculated as follows:

$$Ecorr = E(M - F) - [E(Mghost + F) + E(Fghost + M)] \qquad (2)$$

To analyze the nature of bonding between the target molecule and IRMOF-1(Be), the atoms in molecules (AIM) theory [61] was applied to calculate the geometrical and topological characteristics of the interactions. AIM is a technique used to study the topologies of the electron density ($\rho(r)$) obtained between atoms within a molecule. It has been shown that H-bonding can be identified by the properties of the electron density associated with the bonded moiety. This theory offers a rigorous way of partitioning any system into its atomic fragments, considering the gradient vector field of its electron density. By means of a topological analysis of the electron density, features such as bond critical points and paths of maximum electron density can be utilized to draw a molecular graph (i.e., the network of bond paths that connects linked atoms). In particular, a hydrogen bond is evidenced in the charge density by a bond path linking the proton and the acceptor atom. Popelier [62, 63] suggested criteria for the existence of hydrogen bonding based on the topological properties of the electronic density and a set of integrated properties related to the hydrogen atom. The bond critical points (BCPs), $\rho(r)$, and the eigenvalues of the Hessian of the charge density at the critical point were obtained using the AIM2000 (Version 1.0) program [64]. The measured features used to characterize the hydrogen bonds are $\rho(r)$ and the Laplacian of the charge density at the BCP, $\nabla^2\rho(r)$.

The influence of the adsorption (molecule-surface interactions) on the polarization of the target molecule was also investigated using the analysis of the maps of electrostatic potential (MEPs). The electrostatic potential (EP) is a physically observable quantity that can be derived directly from the wave function. The important role that EP plays in computational chemistry, is indicated by its many applications (predicting sites and relative reactivity toward electrophilic attack, and hydrogen bonding interactions [65, 66]), in reactivity, electrostatic catalysis [67], zeolites [68], and more generally crystal surfaces and cavities. MEPs were obtained using the Molekel program package [69]. With Molekel one can map the EP onto the electronic density based on the atomic charges.
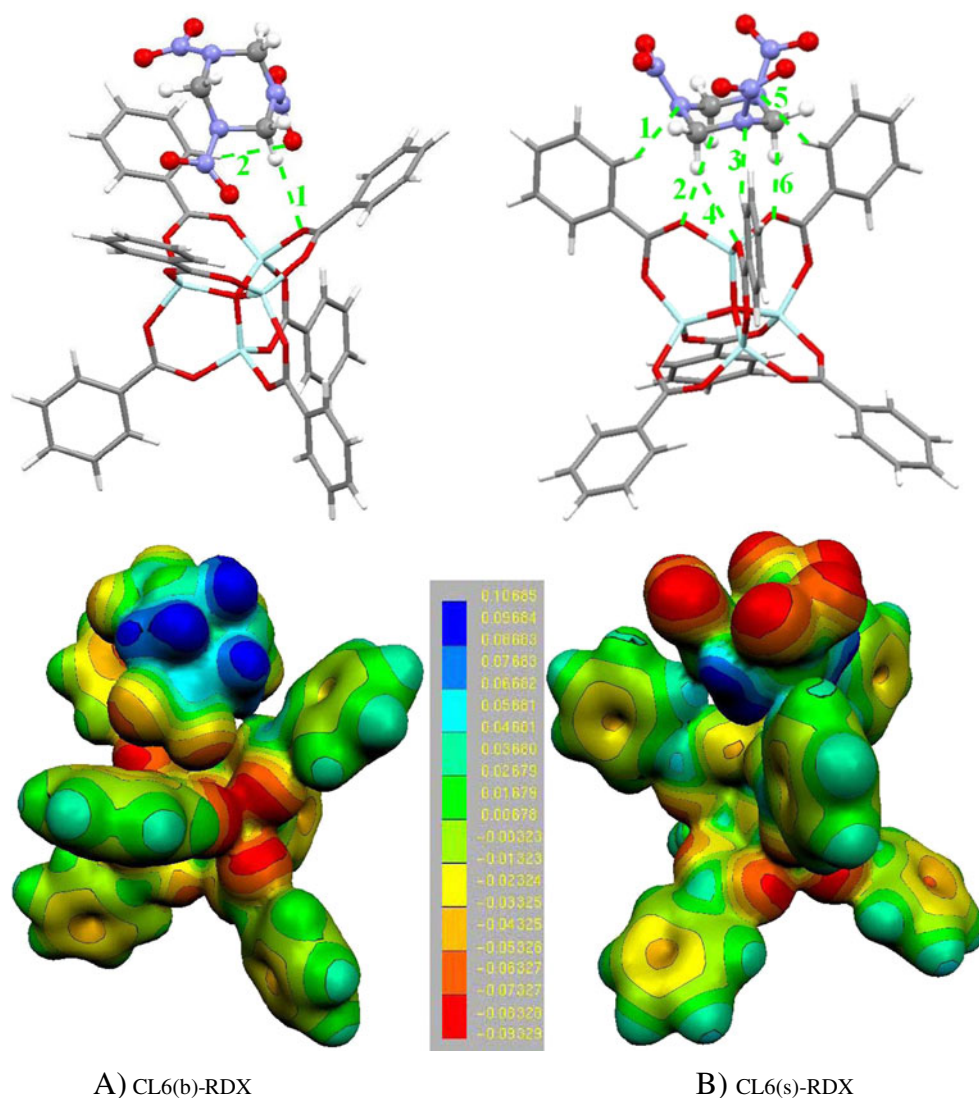
Due to the fact that many questions related to the hydration of MOFs remain unanswered (such as the influence of hydration on the adsorbent-adsorbate interactions, dependence of adsorption on the features of sorption sites, their chemical nature and cage size in the presence of water) we have also

studied the adsorption of RDX and TATP on hydrated IRMOF-1(Be) fragments. The method of microsolvation was applied (addition of one water molecule into the model). Because water is quite polar and the major components of the MOF fragments are the CO_2 groups (with significant quadrupole moment) the presence of water should have a strong impact on the selectivity (involvement) of the CO_2 groups in the interactions with the adsorbates. Therefore, special attention was paid to the water position and several initial locations were modeled. For these complexes W will be added into the notations of hydrated ones.

Results and discussion

The optimized structures of RDX- and TATP-IRMOF-1(Be) calculated at the B97-D/6-31G(d) level are displayed in Figs. 3, 4, 5, 6 denoted as CL6(b) and CL6(s). The results of the AIM analysis are given in Tables 1 and 4 with

geometrical parameters of formed H-bonds. The interaction energy values and the BSSE values obtained at the same level of theory are presented in Tables 2 and 5.

Adsorption of RDX on IRMOF-1(Be)

Intermolecular interactions

Because there are several binding modes of RDX, two different structures of RDX interacting with the CL6 cluster were found. Figure 3 illustrates the optimized structure of RDX interacting with the big (A, CL6(b)-RDX) and small cage (B, CL6(s)-RDX) of the IRMOF-1(Be) cluster.

The position of RDX above the cages varies (it relates to different intermolecular interactions). RDX in its optimized structure interacting with CL6(b) is oriented with the oxygen from the nitro group pointing toward the middle of the Be-Be-Be triangle. RDX binding is mediated only partially by the electrostatic interactions between this oxygen, carbonyl

Fig. 3 The optimized structure of RDX interacting with the big (A, CL6(b)-RDX) and small (B, CL6(s)-RDX) cage site of IRMOF-1(Be) fragment (B97-D/6-31G(d)) and their maps of electrostatic potential

A) CL6(b)-RDX   B) CL6(s)-RDX

Fig. 4 The optimized structure of TATP interacting with the big (A, CL6(b)-TATP) and small (B, CL6(s)-TATP) cage site of IRMOF-1(Be) fragment (B97-D/6-31G(d)) and their maps of electrostatic potential


A) CL6(b)-TATP   B) CL6(s)-TATP
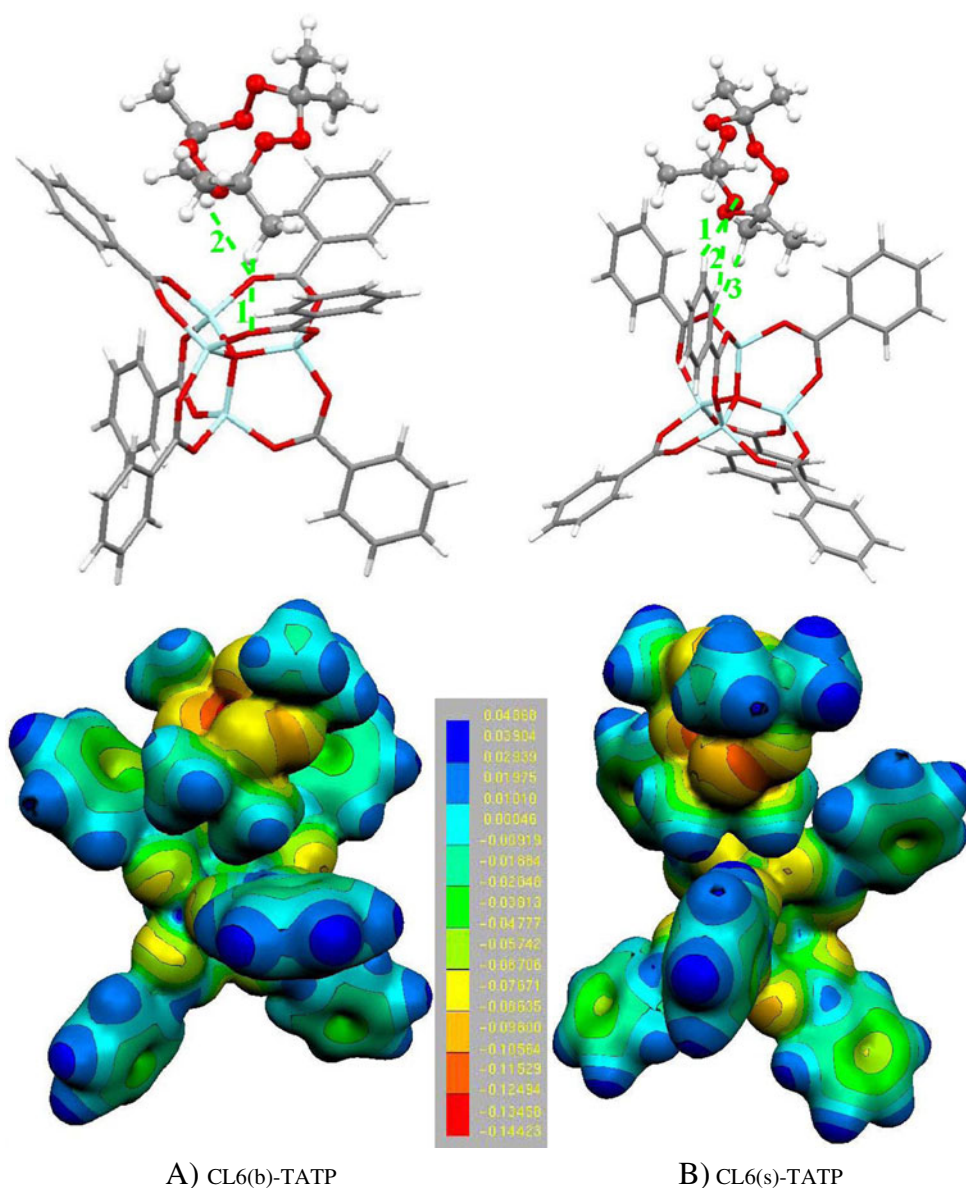
oxygen atoms of all three linkers and Be atoms of the connector (the O…O distances are about 3.1-3.2 Å and Be…O amount from 3.27 through 3.31 to 3.37 Å). The O…O distances are slightly below the sums of the respective van der Waals radii (3.20), which frequently indicates a non-covalent interaction. The theoretical aspects of non-covalent O…O interactions were already established in the literature for various systems, among which are also zeolites [70] and silica [71]. In the systems containing the aromatic nitro derivatives the O…O contacts were suggested to be a consequence of the N…O contacts [72]. Comparable orientation of RDX interacting with IRMOF-1(Zn) was suggested in another theoretical study [35] where Zn-O distance is ~2.0 Å between a Zn atom of connector and $O(N-O_2)$ atom of RDX. The second O atom of the same nitro

group is placed in distance ~3.6 Å from another Zn atom of the same connector.

Two C-H…O H-bridges, between the molecular and linker C-H group and molecular and big cage oxygen atom govern the adsorption. The geometrical and topological characteristics of these H-bonds are presented in Table 1 (HB1 and HB2) and displayed in Fig. 3a (denoted as 1 and 2 in green color). The AIM analysis shows that these C-H…O bonds are quite weak. They are characterized by the H…O distances equal to 2.4-2.5 Å and small ρ and $\nabla^2\rho$ values (0.01 and 0.03 au). The optimized structure of RDX in CL6 (b)(Be)-RDX is similar to that found for RDX interacting with the big cage site of IRMOF-10(Zn) [37].

Only one stable structure containing RDX and CL6(s) fragment was obtained. The RDX C-H groups are oriented toward the middle between two oxygen atoms of two

Fig. 5 The optimized structure of RDX interacting with hydrated big (**A**, CL6(b)W-RDX) and small (**B**, CL6(s)W-RDX) cage site of IRMOF-1 (Be) fragment (B97-D/6-31G (d)) and their maps of electrostatic potential

A) CL6(b)W-RDX   B) CL6(s)W-RDX
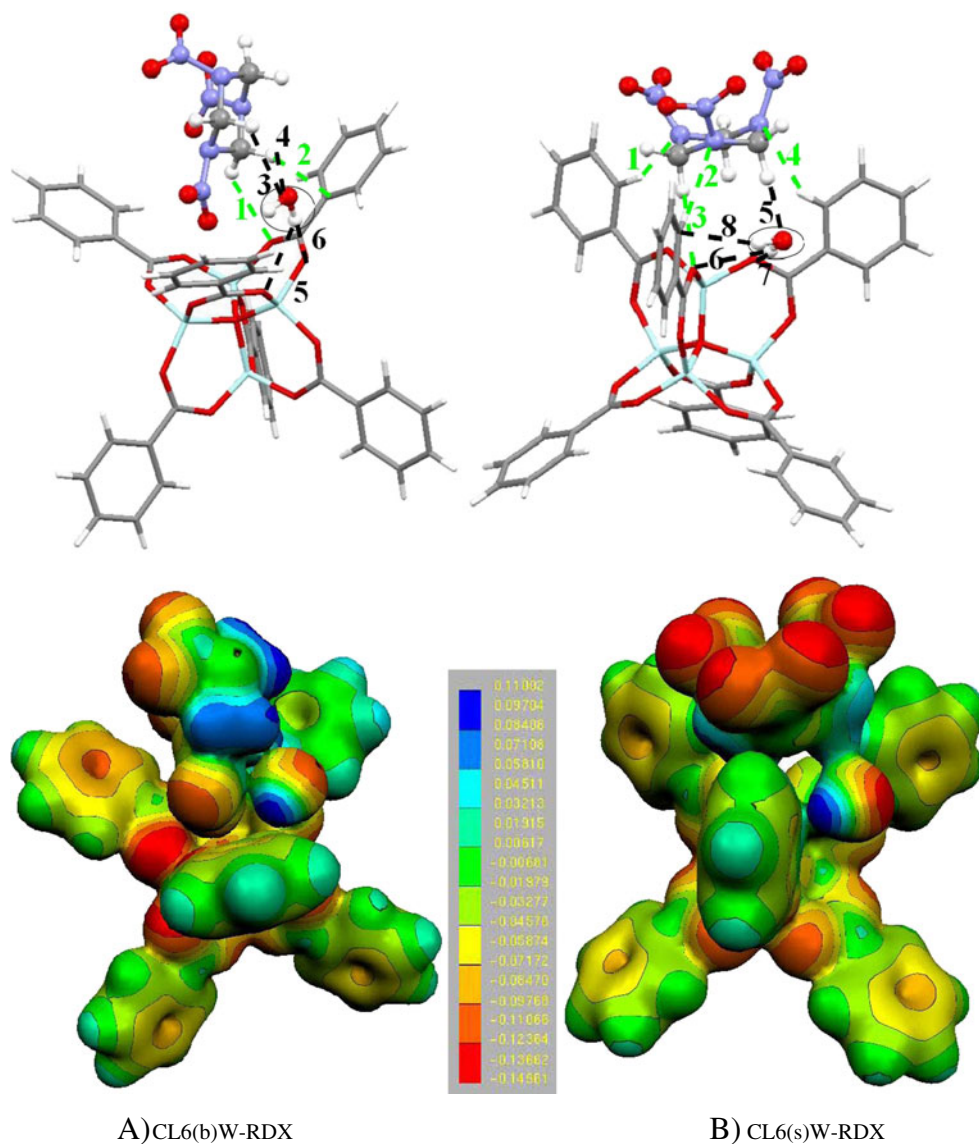
different CO_2 groups. Three of the total six H-bonds are of the C-H…O type (they are denoted HB2, HB4 and HB6 in Table 1 and Fig. 3b) with the C-H groups acting as proton-donors and the oxygen atoms of IRMOF-1(Be) as proton-acceptors. Moreover, the linker C-H groups form three C-H…N H-bridges with the nitrogen atoms of RDX (denoted as HB1, HB3, and HB5 in Table 1 and Fig. 3b). Similarly as in CL6(b)-RDX the H-bridges govern the RDX intermolecular interactions with the IRMOF-1(Be) cluster. The formation of C-H…N mainly stabilizes the adsorbate because C-H…O are much weaker (two times smaller values of ρ and $\nabla^2\rho$ (0.007 au for ρ and 0.025 au for $\nabla^2\rho$) and ~0.3 Å larger H…O distances) as expected. This implies much higher binding affinity of the IRMOF-1(Be) linkers for RDX than the connector shows. The same conclusion was made for RDX interacting with IRMOF-1(Zn) [36, 44] with similar

intermolecular binding between RDX and the IRMOF-1(Zn) models (multiple C-H…O H-bridges).

Energetics

The interaction energy of CL6(b)-RDX given in Table 2 (-8.3 kcal mol^{-1}) indicates that RDX is physisorbed. This value is close to the binding energy of RDX interacting with IRMOF-1 at infinite dilution (-9.2 kcal mol^{-1}) calculated using the grand canonical Monte Carlo (GCMC) simulations [35]. Such small Ecorr value for CL6(b)-RDX demonstrates the presence of only weak polarizing sites in the adsorbing matrix. The opposite situation was investigated for the H_2 adsorption on IRMOF-1(Zn) [22]. The MC simulations identified a high energy binding site for H_2 at the zinc-oxygen corners, which were quickly saturated. But only a small difference was found in the interaction energy values for H_2 binding to benzene or

Fig. 6 The optimized structure of TATP interacting with hydrated big (**A**, CL6(b)W-TATP) and small (**B**, CL6(s)W-TATP) cage site of IRMOF-1 (Be) fragment (B97-D/6-31G (d)) and their maps of electrostatic potential

A) CL6(b)W-TATP

B) CL6(s)W-TATP
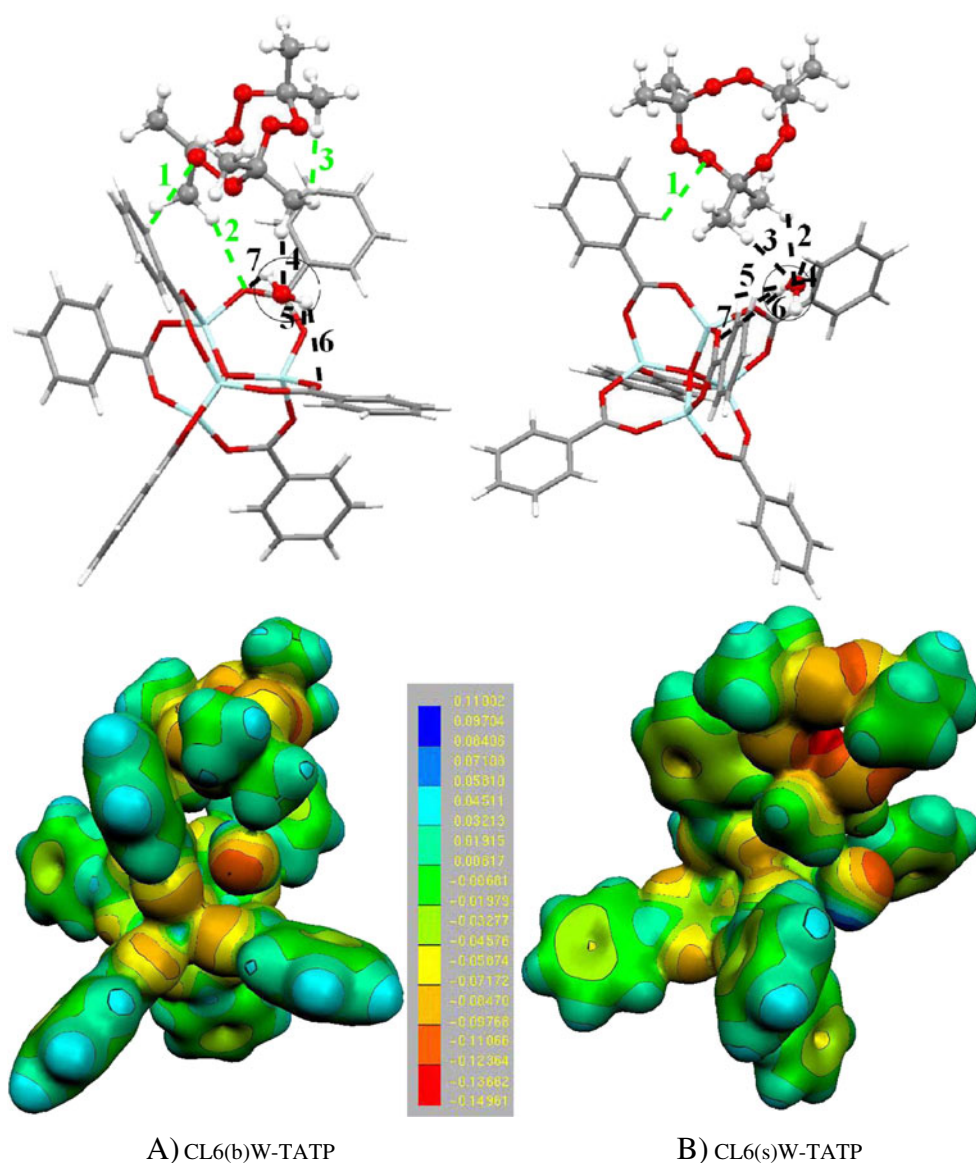
benzenedicarboxylate linker (from -1.1 to -1.2 kcal mol^{-1}) and to zinc-oxygen corners (-1.3 and -1.6 kcal mol^{-1}).

The RDX molecule adsorbs preferably on the small cage of IRMOF-1(Be) as one can see from the formation of six H-bonds in RDX-CL6(s) and larger Ecorr value (-16.4 kcal mol^{-1}). This indicates that the small cage is a better sorption site for RDX (more efficient molecular packing) due to entropic reasons. The MD study [36] shows the same result about the energetically favorable location of RDX interacting with IRMOF-1(Zn). Xiong and co-workers have concluded that the adsorption of RDX is residing (i) in a big cage, (ii) near a vertex, and (iii) between benzene rings [35]. Despite similar modes of RDX binding with CL6(s)(Be) and IRMOF-1(Zn) [38] in the adsorbed phase when the loading of RDX is extremely low, the adsorption strength of these systems vary significantly (-16.4 kcal mol^{-1} vs. -8.1 kcal mol^{-1} for Zn-system). All calculations suggest that whether the

connector fragment of IRMOF-1 contains beryllium or zinc atoms, it affects the orientation and intermolecular interactions between fragment and molecule only slightly. In the case of natural gases the large cages and regions that separate the large and small cages of IRMOF-1, are the preferential adsorption sites [29]. A similar conclusion can also be made about the CO$_2$ storage capacity by MOFs, which is higher with a larger accessible surface area and free volume [73]. This is contrary to our results, which show that the CH groups of linkers oriented directly toward the cage center are favored sites for RDX adsorption (with easier accessibility). This situation occurs when RDX is located above the small cage.

Electrostatic potential analysis

It is well-known that for the adsorption of organic molecules, calculation of MEPs at the surface of a solid material

Table 1 Calculated B97-D/6-31G(d) H…Y and X…Y (in parentheses) distances [Å] and X—H…Y angles [°] and electron density characteristics (ρ [au] and $\nabla^2\rho$ [au]) of RDX-IRMOF-1(Be) systems

Feature	H…Y (X…Y)	X-H…Y	ρ	$\nabla^2\rho$	H…Y (X…Y)	X-H…Y	ρ	$\nabla^2\rho$
System/bond	CL6(b)-RDX				CL6(s)-RDX			
HB1	2.399 (3.436)	158.1	0.010	0.036	2.368 (3.258)	154.0	0.014	0.047
HB2	2.489 (3.32)	144.8	0.008	0.033	2.599 (3.607)	152.1	0.007	0.026
HB3	-	-	-	-	2.360 (3.249)	153.8	0.014	0.047
HB4	-	-	-	-	2.613 (3.611)	150.1	0.007	0.025
HB5	-	-	-	-	2.349 (3.243)	154.7	0.014	0.048
HB6	-	-	-	-	2.625 (3.627)	151.2	0.007	0.025
System/bond	CL6(b)W-RDX				CL6(s)W-RDX			
HB1	2.683 (3.506)	131.9	0.006	0.024	2.361 (3.280)	160.1	0.014	0.046
HB2	2.531 (3.239)	121.1	0.011	0.037	2.564 (3.438)	151.4	0.009	0.033
HB3	2.527 (3.293)	126.4	0.009	0.034	2.454 (3.521)	163.4	0.010	0.033
HB4	2.566 (3.330)	125.7	0.009	0.032	2.512 (3.351)	146.0	0.010	0.035
HB5	2.540 (3.113)	117.4	0.008	0.034	2.165 (3.194)	154.5	0.021	0.055
HB6	2.052 (3.009)	165.6	0.020	0.065	2.424 (3.023)	119.3	0.010	0.041
HB7	-	-	-	-	2.078 (3.028)	164.3	0.020	0.063
HB8	-	-	-	-	2.624 (3.544)	157.1	0.007	0.025

helps to gain knowledge about the sorption processes and can provide better understanding of chemical reactivity of studied systems. The MEPs of the CL6-RDX systems are presented in Fig. 3. Figure 1a displays the MEP of isolated RDX. The values of maximum positive (Vmax) and minimum negative electrostatic potential (Vmin) located above the nitrogen, oxygen, carbon and hydrogen atoms are presented in Table 3. The electrostatic interactions with the IRMOF-1(Be) fragments are physically and thermodynamically favorable. The negative potential is located above the oxygen and nitrogen atoms of isolated and interacting RDX. It should be noted that in contrast to other elements, the nitrogen atoms display very low electron density on the interface surface in all studied RDX complexes. The negative potential located above the oxygen atoms is enhanced for all RDX complexes (about 30 kcal mol^{-1}) compared with isolated RDX. High change of EP implies that the probability of a proton binding to different sites is geometrically blocked without a favored localized region. The most significant increase (about 40 kcal mol^{-1}) is found for the least stable system (CL6(b)-RDX). This shows that the main

factor affecting the negative EP values is position and orientation of the target molecule toward the IRMOF-1 (Be) fragment.

Modification of positive potential (located above the carbon and hydrogen atoms) is similar to that observed for negative Vmin but the effect of the IRMOF-1(Be) fragment is less strong. The carbon and hydrogen ring atoms in CL6-RDX become less positive compared with isolated RDX. In particular, positive Vmax values for the molecular hydrogen atoms in CL6(s)- and CL6(b)-RDX decrease by about 12-20 kcal mol^{-1}. This change is two times lower than that found for negative Vmin located above the oxygen atoms. It is more significant for CL6(s)-RDX due to greater involvement of the C-H groups in the intermolecular interactions. This confirms the conclusion made at the end of the previous paragraph that the placement of the adsorbate influences the EP values the most significantly. The smallest positive Vmax located above the carbon atoms belongs to CL6(b)–RDX. This is the lowest positive Vmax value among all studied RDX-IRMOF-1(Be).

Table 2 BSSE energies (Ese), BSSE uncorrected (Eint) and corrected interaction energies (Ecorr) [kcal mol^{-1}] of RDX-IRMOF-1(Be) calculated at B97-D/6-31G(d)

System/Energy	CL6(b)-RDX	CL6(s)-RDX	CL6(b)W-RDX	CL6(s)W-RDX
Eint	-16.7	-21.3	-20.4	-18.9
Ese	8.4	4.9	8.8	6.0
Ecorr	-8.3	-16.4	-11.6	-12.9

Table 3 The most negative (oxygen and nitrogen, Vmin) and positive (hydrogen and carbon, Vmax) electrostatic potential values [kcal mol^{-1}] for RDX-IRMOF-1(Be) systems

System/atom	CL6(b)-RDX	CL6(s)-RDX	CL6(b)W-RDX	CL6(s)W-RDX	RDX
O	-71.7	-58.5	-58.5	-62.7	-31.4
N	-4.1	-2.0	-3.8	-3.4	-7.5
C	9.4	10.5	16.7	26.3	34.2
H	75.8	67.0	71.4	63.3	87.9

Adsorption of TATP on IRMOF-1(Be)

The optimized structures of TATP interacting with the big (CL6(b)-TATP) and small cage of the IRMOF-1(Be) fragment (CL6(s)-TATP) are presented in Fig. 4. In CL6(b)-TATP two H-bonds between the molecular C-H groups and carbonyl oxygen atoms are responsible for stabilization of the molecule. The AIM analysis given in Table 4 shows that obtained ρ and $\nabla^2\rho$ values of formed H-bridges in CL6(b)-TATP are within the range proposed by Koch and Popelier [62, 63] (mentioned in 3.1.1 section). They are very weak with H…O distances in the range 2.58-2.67 Å and quite small ρ and $\nabla^2\rho$ (0.006-0.008 au and 0.023-0.032 au). Due to the orientation of the adsorbate toward the CL6(b) fragment, one could expect formation of more than two C-H…O H-bridges. However, the AIM analysis does not confirm this assumption.

In the CL6(s) fragment, both the proton acceptor and proton donor groups are favorable for the TATP adsorption. Due to this fact, in CL6(s)-TATP the formation of three C-H…O H-bridges occurs with participation of two molecular and one fragmental oxygen. Similarly as for CL6(b)-TATP, the H…O and C…O distances are quite long (2.5-2.64 and 3.3-3.5 Å). The electron density and the Laplacian of the electron density are characterized by values proportional to these distances. For example, the strongest H-bridge (HB1) corresponds with the largest ρ (0.009 au) and $\nabla^2\rho$ (0.034 au). The longest H…O distance (found for HB3, 2.64 Å) concurs with the smallest ρ (0.006 au) and $\nabla^2\rho$ (0.023 au). The TATP stable configurations with IRMOF-8(Zn) at room temperature [39] were revealed to be analogous to that found for TATP-CL6(Be) (TATP migrates toward the center of the IRMOF-8 cage into a similar position as found for the Be complexes). However, at zero temperature TATP was shown to remain inert to interactions with IRMOF-8.

The binding energy of CL6(b)-TATP (-10.7 kcal mol^{-1}) is enhanced by about 2 kcal mol^{-1} (see Table 5) compared with CL6(s)-TATP and CL6(b)-RDX. On the other hand, formation of CL6(b)-TATP is about two times less effective than the formation of CL6(s)-RDX. This situation may account for larger activation of the oxygen atoms of the big cage fragment (CL6(b)) when connected with TATP and oxygen atoms of the small cage (CL6(s)) when interacting with RDX. The binding enthalpies of hydrogen adsorbed on IRMOF-1(Zn) are much smaller (from 0.5 to 0.8 kcal mol^{-1}) [23]. It was concluded that the adsorptive properties of this material are mainly produced by dispersive interactions with the internal wall structure and by weak electrostatic forces associated with $O_{13}Zn_4$ clusters. This suggests the key role of the atoms neighboring the active site. Therefore, we conclude that the large difference in structures and adsorption energies of the RDX- and TATP-IRMOF-1 complexes can be attributed to differences in the MOF fragment's active site and molecular groups involved in the interactions.

Electrostatic potential analysis

The MEPs of the CL6-TATP systems are illustrated in Fig. 4. Figure 1b displays the MEP of isolated TATP. The values of the minimum negative EP (Vmin) located above the oxygen atoms and carbon atoms and maximum positive EP (Vmax) located above the hydrogen atoms are presented in Table 6. The electron density distribution is such that due to local accumulations of electrons (as, for example, in lone pair regions) negative EP located above oxygen atoms is increased. This finding agrees well with increase of the negative EP above molecular oxygen atoms in the CL6(Be)-RDX complexes. For TATP acting as a proton acceptor, the presence of a lone pair (suitable for the formation of a H-bond) on the O atoms concurs with a local minimum in

Table 4 Calculated (B97-D/6-31G(d)) H…Y and X…Y (in parentheses) distances [Å], X—H…Y angles [°] and electron density characteristics (ρ [au] and $\nabla^2\rho$ [au]) of TATP-IRMOF-1(Be) systems

Feature	H…Y (X…Y)	X-H…Y	ρ	$\nabla^2\rho$	H…Y (X…Y)	X-H…Y	ρ	$\nabla^2\rho$
System/bond	CL6(b)-TATP				CL6(s)-TATP			
HB1	2.580 (3.432)	134.0	0.008	0.032	2.524 (3.248)	132.2	0.009	0.034
HB2	2.660 (3.479)	173.2	0.006	0.023	2.534 (3.354)	143.4	0.008	0.031
HB3	-	-	-	-	2.639 (3.529)	137.9	0.006	0.024
System/bond	CL6(b)W-TATP				CL6(s)W-TATP			
HB1	2.650 (3.095)	108.8	0.008	0.033	2.625 (3.283)	126.0	0.007	0.029
HB2	2.537 (3.488)	144.9	0.008	0.030	2.515 (3.353)	132.3	0.008	0.031
HB3	2.603 (3.643)	158.1	0.008	0.029	2.543 (3.471)	141.6	0.009	0.032
HB4	2.483 (3.233)	124.5	0.010	0.036	2.659 (3.360)	130.3	0.006	0.028
HB5	2.450 (3.160)	129.6	0.010	0.039	2.657 (3.359)	130.2	0.007	0.033
HB6	2.233 (3.196)	115.0	0.006	0.029	2.153 (3.087)	160.0	0.016	0.054
HB7	2.509 (3.106)	119.5	0.009	0.037	2.473 (3.087)	120.6	0.009	0.035

Table 5 BSSE energies (Ese), BSSE uncorrected (Eint) and corrected interaction energies (Ecorr) [kcal mol^{-1}] of TATP-IRMOF-1(Be) calculated at B97-D/6-31G(d)

System/ Energy	CL6(b)-TATP	CL6(s)-TATP	CL6(b)W-TATP	CL6(s)W-TATP
Eint	-17.1	-12.2	-15.6	-11.2
Ese	6.4	3.7	6.2	4.4
Ecorr	-10.7	-8.5	-9.4	-6.8

negative EP (Vmin amounts to -72 (CL6(s)-TATP) and -86 kcal mol^{-1} (CL6(b)-TATP)). On the other hand, the oxygen atoms of the CL6 fragment do not donate to a positive potential region of the C-H groups of TATP. Thus, the positive EP above hydrogen atoms is slightly decreased in comparison with isolated TATP (about 1-4 kcal mol^{-1}). This situation is more significant in CL6(s)-TATP. It demonstrates that placement of TATP above the small cage affects more significantly the redistribution of positive EP while for TATP located above the big cage, the negative EP is changing to a larger extent. This situation is consistent with the results obtained for CL6(Be)-RDX. The largest difference between the positive EP values of TATP and RDX occurs for hydrogen atoms (about 40 kcal mol^{-1}) and between the negative EP values corresponds to carbon atoms (about 30 kcal mol^{-1}). This is attributable to the fact that carbon atoms in the TATP complexes are characterized by negative EP, which is largely lower (3-4 times) than the Vmin values for oxygen atoms.

Adsorption of RDX and TATP on hydrated IRMOF-1(Be)

In order to test the influence of hydration on the interactions of RDX and TATP with IRMOF-1(Be) fragments, one water molecule was added into the system in several initial orientations. The optimized structures of the target molecule adsorbed on hydrated CL6W(Be) are given in Figs. 5 and 6. Tables 1 and 4 present the characteristics of formed intermolecular interactions as obtained from the AIM analysis.

Table 6 The most negative (oxygen and carbon, Vmin) and positive (hydrogen, Vmax) electrostatic potential values [kcal mol^{-1}] for TATP-IRMOF-1(Be) systems

System/ atom	CL6(b)-TATP	CL6(s)-TATP	CL6(b)W-TATP	CL6(s)W-TATP	TATP
O	-85.9	-72.3	-86.1	-69.4	-64.2
C	-22.4	-23.9	-11.8	-12.4	-37.2
H	33.6	30.5	21.2	20.2	34.8

A water molecule in all CL6W(Be) complexes is strongly attracted to the cage oxygen atoms. It moves slightly away from the adsorbate, converging in particular to two different configurations in CL6W-TATP, but only into one in CL6W-RDX. In the first position, which is found in three systems, water is placed on the corner of the cage closer to the adsorbent's oxygen atoms with one hydrogen pointed toward two of the oxygen atoms (Figs. 5a, b and 6b). In this location one hydrogen atom of water is placed about 2.1-2.5 Å from the cage oxygen atoms and the Ow-Hw-O angle amounts to 120-165°. In the second configuration, found for CL6(b)W-TATP (Fig. 6a), water remains above the middle of the cage in equal distance from the fragment and TATP molecule. In this location both hydrogen atoms of water are oriented parallel with the cage surface close to the oxygen atoms of the cage (Hw…Os distance is 2.2-2.5 Å) and the Ow-Hw-O angles vary from 115 to 130°.

In both configurations water interacts via multiple H-bridges with the MOF fragment and target molecules. The number of formed H-bonds differs based on molecule and cage type. In CL6(b)W-RDX (HB3 and HB4 in Table 1 and Fig. 5a) and CL6(s)W-TATP (HB2 and HB3 in Table 4 and Fig. 6b) water's oxygen atom forms two H-bonds with the adsorbate's C-H groups. However, in CL6(s)W-RDX (HB5 in Table 1 and Fig. 5b) and CL6(b)W-TATP (HB4 in Table 4 and Fig. 6a) only one such interaction is created. They are quite weak (in all systems having H…O distances ~2.5 Å and the ρ and $\nabla^2\rho$ values 0.01 and 0.03 au) with an exception of one stronger Ow…H-C in CL6(s)W-RDX (HB5, H…O is 2.17 Å and ρ and $\nabla^2\rho$ are 0.02 and 0.055 au). The rest of the H-bonds in which water is involved, are created with the oxygen atoms of the IRMOF-1(Be) fragment. They are mostly of Ow-Hw…O type except two Ow…H-C H-bridges in CL6(s)W-TATP (formed with the linker C-H groups, HB4 and HB5 in Table 4 and Fig. 6b), which are weaker (~0.1 longer H…O distances) than Ow-Hw…O. Such H-bonding between water and IRMOF-1 oxygen atoms is suggested in a study by Hafizovic et al. [74]. Physisorption of water with IRMOF-1 is also observed experimentally [75]. The authors concluded that for low water content, no reaction occurs and the IRMOF-1 structure is maintained.

Adsorbed RDX and TATP form the same type of interactions with CL6(W) as with the non-hydrated MOF(Be) fragments. Therefore, the intermolecular binding will be described only briefly to highlight the differences. In hydrated systems due to presence of water some intermolecular interactions, which occurred in non-hydrated systems, are blocked. In CL6(s)W-RDX only one slightly stronger C-H…O H-bond is formed between the molecular CH group and cage oxygen (instead of three such bonds found in CL6(s)-RDX). It is characterized by 0.15 Å shorter H…O distance and 0.003 and 0.008 au larger ρ and $\nabla^2\rho$ values (HB3 in Table 1 and in

Fig. 5b). On the other hand, the C-H…N interactions (between molecular nitrogen and fragmental CH groups) are less strong in hydrated CL6(s)W-RDX (HB1, HB2 and HB4 in Table 1 and Fig. 5b). The situation is slightly different for RDX interacting with CL6(b)W, where the same number of H-bonds is formed (HB1 and HB2 in Table 1 and Fig. 5a). They are of C-H…O and C-H…C type between the molecular CH group and oxygen atom of the CO_2 group and linker's carbon atom. The ρ and $\nabla^2\rho$ values show that despite longer C…H distance, the C-H…C interaction is stronger than C-H…O H-bonds in non-hydrated complex.

TATP interactions with hydrated CL6W(Be) differ again in binding strength, which is lower than revealed for the non-hydrated complexes. In CL6(s)W-TATP only one C-H…O H-bond is created (HB1 in Table 4 and Fig. 6b, between the linker C-H group and molecular oxygen) compared with three C-H…O bonds found in CL6(s)-TATP. This is accompanied by lower ρ and $\nabla^2\rho$ values (~0.002 and 0.005 au) and enlarged H…O distance (0.1 Å). The AIM analysis shows that the only exception with larger number of H-bonds is the CL6(b)W-TATP complex (one additional C-H…C type between molecular CH group and linker's carbon, denoted HB3 in Table 4 and Fig. 6a). However, this interaction is quite weak (2.6 Å H…O distance and 0.08 au value of the electron density) and does not lead to an increase of the adsorption affinity of TATP toward the big cage of IRMOF-1(Be).

Energetics

Despite the existence of direct interactions between water and target molecule, the results show the energy loss for one RDX and both TATP systems (see Tables 2 and 5 for more details). This is due to changes in the intermolecular interactions induced by water adsorption. Another reason can be the steric effect of additional water, which causes the MOF fragment to be less active in interacting with RDX and TATP than in non-hydrated cases. This results in about 1 kcal mol^{-1} smaller Ecorr value for TATP systems and to about 4 kcal mol^{-1} for CL6(s)-RDX. In the case of CL6(b)W-RDX, the presence of water stabilizes RDX by about 3 kcal mol^{-1} due to formation of two strong H-bonds between water and molecule. This finding agrees well with predictions from molecular simulation studies of adsorption of natural gases in IRMOF-1 [29]. The authors suggested decrease of IRMOF-1 storage capacity due to water content and reduction of adsorption due to shielding of the binding sites (favored for interactions with the adsorbates) by water. Exposure to more than 4% water causes collapsing of the IRMOF-1 framework [75].

It can be generally concluded that RDX and TATP interact more strongly with the non-hydrated than with the hydrated IRMOF-1(Be) surface. This difference is larger for RDX systems and depends on the position and orientation of the target molecule toward the MOF fragment. The presence of big or small cage controls the interactions of water with the MOF fragment and the target molecule. Therefore, the results vary for all four studied systems. This means that the difference in the Ecorr values is about 10-20% if one compares TATP systems and 20-30% if the CL6-RDX and CL6W-RDX complexes are considered. The interaction energy values are in line with the nature of the adsorption. The binding energies of CL6(b)-TATP and CL6(s)-RDX are in the order of one and two additional H-bridges between the adsorbate and surface compared with the hydrated ones.

Electrostatic potential analysis

MEPs of hydrated complexes are depicted in Figs. 5 and 6 and the minimum negative (Vmin) and maximum positive EP values (Vmax) are given in Tables 3 and 6. The adsorption does not change the fact that the molecular negative EP lows are located above the oxygen atoms and positive highs above hydrogen atoms in all hydrated systems. Only Vmin values and potential redistribution are modified due to different participation of the molecular groups in H-bridges with the CL6(Be)W fragments.

The MEPs of hydrated RDX and TATP complexes gave slightly different picture for the molecular charge compared to corresponding non-hydrated systems. The polarization strength of the interactions is partially lost with the addition of water (only exception is CL6(b)-RDX). The largest difference in Vmin between non-hydrated and hydrated complexes is observed for oxygen atoms in CL6(b)W-RDX (about 15 kcal mol^{-1} decrease). Differences for the rest of the hydrated systems with both adsorbates are less than 5 kcal mol^{-1}. This indicates smaller charge redistribution for the molecular oxygen atoms in CL6(b)W-RDX than in CL6(b)-RDX. This partially confirms the statements in Sect. "Energetics" related to differences in the Ecorr values. In CL6W-TATP larger modification of EP was found for carbon and hydrogen atoms (10-12 kcal mol^{-1}) than revealed for oxygen atoms.

The EP of the IRMOF-1(Be) surface changes insignificantly due to addition of water for the RDX systems. This agrees well with the statement of Novakovic et al. [76] regarding the change in the EP value near the ligand for [Zn(CH$_5$N$_3$S)$_2$](NO$_3$)$_2$] complex. Moreover, for IRMOF-1 was suggested [74] that the existence of water does not affect directly the coordinative sphere of this material. The authors predicted that the presence of H-bonding between water and the first shell oxygen is the cause of small modifications of IRMOF-1. In the TATP complexes addition of water largely decreases the

Vmax values of the positive EP located above the fragment hydrogen atoms (about 30 kcal mol^{-1}). The negative EP lows in CL6W-RDX appear at the oxygen atoms of the CO$_2$ group (Vmin equals to 53-62 kcal mol^{-1}) while in CL6W-TATP the negative Vmin values remain the largest above the molecular oxygen atoms.

Closer analysis of the EP supports the facts discussed above related to the nature of the RDX and TATP adsorption (it leads to structural change of the adsorbates, and modification of both the topology and value of the electrostatic potential). The MEPs show preferable binding of positively charged C-H groups of RDX (Vmin located above carbons is 17-26 kcal mol^{-1} and Vmax above hydrogen atoms is 63-71 kcal mol^{-1}) with strong negative basins located above small cage oxygen atoms than with such sites of the big cage. On the other hand, due to the TATP character (negative EP occurs above both molecular oxygen and carbon atoms) its MEP is affected more significantly by the presence of strong negative sites of CL6(b)W. This supports the statements about changes in the adsorption strength for RDX and TATP hydrated systems made in Sect. "Energetics" (increase for CL6(b)W-RDX, decrease for the rest of the complexes).

Conclusions

The adsorption of the RDX and TATP molecules with IRMOF-1(Be) fragments has been studied because the relation between the high explosive molecules and their binding strength with MOFs remains an open question. The B97-D/6-31G(d) level of theory was applied. The results presented here provide a comprehensive picture of RDX and TATP chemistry with hydrated and non-hydrated IRMOF-1(Be).

The calculations indicate that RDX binds preferentially with the small cage site, while TATP interacts slightly stronger with the big cage site of IRMOF-1(Be). This can be attributed to entropic effects, which can cause different efficiency of these sites in molecular packing. Thus, it can be inferred that due to such characteristics of IRMOF-1 (presence of two different sorption sites) strong adsorption selectivity can be induced. The binding occurs due to the formation of multiple hydrogen bonds, which lock TATP and RDX in fixed interacting geometries. The H-bridges are created mainly between the C-H groups of TATP and the cage oxygen atoms. In the case of RDX, the molecular C-H groups and nitrogen atoms bind preferentially with the fragmental C-H groups and oxygen atoms. The adsorbates are additionally stabilized by weak electrostatic interactions between the NO$_2$ groups of RDX, oxygen atoms of TATP and IRMOF-1 oxygen atoms and beryllium.

The binding strength of the RDX- and TATP-IRMOF-1(Be) complexes is largely determined by the properties of the anchor groups of this material. Generally, the energetic stability of RDX complexes is greater than for TATP systems. CL6(s)-RDX, in which RDX forms the largest number of H-bridges with the MOF fragment, is the most stable (the interaction energy amounts to about 16 kcal mol^{-1}). The preferred adsorption sites were confirmed by calculations of the values of electrostatic potential and analysis of changes of electronic structure of the RDX- and TATP-IRMOF-1(Be) complexes.

An important finding of this study is that the binding is more favored with non-hydrated IRMOF-1(Be) fragments. The addition of water destabilizes adsorbates due to steric effects (shielding of the binding sites favored for interactions with RDX and TATP). The only exception is RDX interacting with the big cage model because of the formation of two strong H-bridges with water. We determined the nature of the hydrated adsorption. This is mediated by H-bridges of the adsorbate partially with MOF and partially with water. In all studied systems, water is favorably located above the big cage. It is placed in two different orientations. Both of them are close to the cage oxygen atoms, with which it forms multiple H-bond type interactions. A larger amount of water molecules interacting with IRMOF-1 in the presence of RDX and TATP will be the subject of our future study to find how different amounts affect the IRMOF-1 structure and interactions with the adsorbates.

This work provides qualitative and quantitative insight into the nature of intermolecular interactions between RDX, TATP and non-hydrated and hydrated IRMOF-1 fragments. The conclusions should be transferable to other explosive-MOFs systems. It also highlights the challenges confronting the design of highly specific MOFs structures that can be used as preconcentrators for explosive contaminants to simplify their detection.

References

1. Hiyoshi RI, Nakamura J, Brill TB (2007) Propellants, explosives. Pyrotechnics 32:127–134

2. Kaye SM (ed) (1978) Encyclopedia of explosives and related items. PATR 2700 Vol. 8. U.S. Army Armament Research & Devlop. Comp: Dover, NJ, 203

3. Hon DNS (1985) Pulp & Paper Canada 1985, 86:129–131

4. Reutter DJ, Bender ED, Rudolph RL (1983) Proceed Int Symp Analysis & Detection of Explosives. U.S. Dept. Justice. FBI, Quantico, VA, p 149

5. Zitrin S, Kraus S, Glattstein B (1983) Proceed Int Symp Analysis & Detection of Explosives, US Dept. Justice. FBI, Quantico, VA, p 137

6. Swadley MJ, Li T (2007) J Chem Theor Comput 3:505–513

7. Chakraborty D, Muller RP, Dasgupta S, Goddard WA (2000) J Phys Chem A 104:2261–2272

8. Boyd S, Gravelle M, Politzer P (2006) J Chem Phys 124:104508–104517

9. Harris NJ, Lammertsma K (1997) J Am Chem Soc 119:6583–6589

10. Rice BM, Chabalowski CF (1997) J Phys Chem A 101:8720–8726

11. Chae HK, Siberio-Perez DY, Kim J, Go Y, Eddaoudi M, Matzger AJ, O'Keeffe M, Yaghi OM (2004) Nature 427:523–527

12. Eddaoudi M, Kim J, Rosi N, Vodak D, Wachter J, O'Keefe M, Yaghi OM (2002) Science 295:469–472

13. Huang L, Wang H, Chen J, Wang Z, Sun J, Zhao D, Yan Y (2003) Microporous Mesoporous Mater 58:105–114

14. Kepert CJ, Rosseinsky MJ (1999) J Chem Soc Chem Commun 4:375–376

15. Tafipolsky M, Amirjalayer S, Schmid R (2007) J Comput Chem 28:1169–1176

16. Mattesini M, Soler J, Yndurain F (2006) Phys Rev B 73:094111–094112

17. Li H, Eddaoudi M, O'Keeffe M, Yaghi OM (1999) Nature 402:276–279

18. Rosi NL, Eckert J, Eddaoudi M, Vodak DT, Kim J, O'Keeffe M, Yaghi OM (2003) Science 300:1127–1129

19. Yaghi OM, O'Keeffe M, Ockwig NW, Chae HK, Eddaoudi M, Kim J (2003) Nature 423:705–714

20. Fuentes-Cabrera M, Nicholson DM, Sumpter BG, Widom M (2005) J Chem Phys 123:124713–124715

21. Hausdorf S, Baitalow F, Bohle T, Rafaja D, Mertens FORL (2010) J Am Chem Soc 132:10978–10981

22. Sagara T, Klassen J, Ganz E (2004) J Chem Phys 121:12543–12547

23. Bordiga S, Vitillo JG, Ricchiardi G, Regli L, Cocina D, Zecchina A, Arstad B, Bjørgen M, Hafizovic J, Lillerud KP (2005) J Phys Chem B 109:18237–18242

24. Yang QY, Zhong CL (2005) J Phys Chem B 109:11862–11864

25. Belof JL, Stern AC, Eddaoudi M, Space B (2007) J Am Chem Soc 129:15202–15210

26. Han SS, Goddard WA III (2007) J Am Chem Soc 129:8422–8423

27. Rowsell JLC, Millward AR, Park KS, Yaghi OM (2004) J Am Chem Soc 126:5666–5667

28. Rowsell JLC, Eckert J, Yaghi OM (2005) J Am Chem Soc 127:14904–14910

29. Martín-Calvo A, García-Pérez E, Castillo CM, Calero S (2008) Phys Chem Chem Phys 10:7085–7091

30. Dubbeldam D, Frost H, Walton KS, Snurr RQ (2007) Fluid Phase Equilibria 261:152–161

31. Amirjalayer S, Schmid R (2009) Microporous Mesoporous Mater 125:90–96

32. Moellmer J, Celer EB, Luebke R, Cairns AJ, Staudt R, Eddaoudi M, Thommes M (2010) Microporous Mesoporous Mater 129:345–353

33. Wells BA, Liang Z, Marshall M, Chaffee AL (2009) Energ Proc 1:1273–1280

34. Pawsey S, Moudrakovski I, Ripmeester J, Wang LO, Exarhos GJ, Rowsell JLC, Yaghi OM (2007) J Phys Chem C 111:6060–6067

35. Xiong R, Fern JT, Keffer DJ, Fuentes-Cabrera MA, Nicholson DM (2009) Mol Simul 35:910–919

36. Odbadrakh K, Lewis JP, Nicholson DM, Petrova T, Michalkova A, Leszczynski J (2020) J Phys Chem C 114:3732–3736

37. Xiong R, Keffer DJ, Fuentes-Cabrera M, Nicholson DM, Michalkova A, Petrova T, Leszczynski T, Odbadrakh K, Doss BL, Lewis JP (2010) Langmuir 26:5942–5950

38. Xiong R, Odbadrakh K, Michalkova A, Luna JP, Petrova T, Keffer DJ, Nicholson DM, Fuentes-Cabrera MA, Lewis JP, Leszczynski J (2010) Sens Actuators B Chem 143:459–468

39. Odbadrakh K, Lewis JP, Nicholson DM (2010) J Phys Chem C 114:7535–7540

40. Dubnikova F, Kosloff R, Zeiri Y, Karpas Z (2002) J Phys Chem A 106:4951–4956

41. Munoz RAA, Lu D, Cagan A, Wang J (2007) Analyst 132:560–565

42. Schulte-Ladbeck R, Vogel M, Karst U (2006) Anal Bioanal Chem 386:559–565

43. Efremenko I, Zach R, Zeiri Y (2007) J Phys Chem C 111:11903–11911

44. Petrova T, Michalkova A, Leszczynski J (2009) Struct Chem 21:391–404

45. Burrows AD, Cassar K, Friend RMW, Mahon MF, Rigby SP, Warren JE (2005) Cryst Eng Comm 7:548–550

46. Schröck K, Schröder F, Heyden M, Fischer RA, Havenith M (2008) Phys Chem Chem Phys 10:4732–4739

47. Frisch MJ, Trucks GW, Schlegel HB, Scuseria GE, Robb MA, Cheeseman JR, Scalmani G, Barone V, Mennucci B, Petersson GA, Nakatsuji H, Caricato M, Li X, Hratchian HP, Izmaylov AF, Bloino J, Zheng G, Sonnenberg JL, Hada M, Ehara M, Toyota K, Fukuda R, Hasegawa J, Ishida M, Nakajima T, Honda Y, Kitao O, Nakai H, Vreven T, Montgomery JA Jr, Peralta JE, Ogliaro F, Bearpark M, Heyd JJ, Brothers E, Kudin KN, Staroverov VN, Kobayashi R, Normand J, Raghavachari K, Rendell A, Burant JC, Iyengar SS, Tomasi J, Cossi M, Rega N, Millam NJ, Klene M, Knox JE, Cross JB, Bakken V, Adamo C, Jaramillo J, Gomperts R, Stratmann RE, Yazyev O, Austin AJ, Cammi R, Pomelli C, Ochterski JW, Martin RL, Morokuma K, Zakrzewski VG, Voth GA, Salvador P, Dannenberg JJ, Dapprich S, Daniels AD, Farkas Ö, Foresman JB, Ortiz JV, Cioslowski J, Fox DJ (2009) Gaussian 09, Revision A.1. Gaussian Inc. Wallingford, CT

48. Parr RG, Yang W (1989) Density-functional theory of atoms and molecules. Oxford Univ Press, Oxford

49. Grimme S (2006) J Comput Chem 27:1787–1799

50. Zhidomirov GM, Shubin AA, Milov MA, Kazansky VB, van Santen RA, Hensen EJM (2008) J Phys Chem C 112:3321–3326

51. Yuan S, Shi W, Li B, Wang J, Jiao H, Li YW (2005) J Phys Chem A 109:2594–2601

52. Castella-Ventura M, Akacem Y, Kassab E (2008) J Phys Chem C 112:19045–19054

53. Soscun H, Castellano O, Hernandez J (2004) J Phys Chem B 108:5620–5626

54. Pelmenschikov A, Leszczynski J (1999) J Phys Chem B 103:6886–6890

55. Gorb L, Lutchyn R, Zub Y, Leszczynska D, Leszczynski D (2006) Theochem 766:151–157

56. Gorb L, Gu J, Leszczynska D, Leszczynski J (2000) Phys Chem Chem Phys 2:5007–5012

57. Michalkova A, Szymczak JJ, Leszczynski J (2005) Struct Chem 16:325–337

58. Sauer J (1989) Chem Rev 89:199–255

59. Sauer J, Ugliengo P, Garrone E, Saunders VR (1994) Chem Rev 94:2095–2160

60. Boys SF, Bernardi F (1970) Mol Phys 19:553–566

61. Bader RWF (1990) Atoms in Molecules: A Quantum Theory. Oxford University Press, Oxford
62. Koch U, Popelier PLA (1995) J Phys Chem 99:9747–9754
63. Popelier PLA (1998) J Phys Chem A 102:1873–1878
64. Biegler-König F, Schönbohm J, Bayles D (2001) J Comput Chem 22:545–559
65. Muñoz-Caro C, Niño A, Sement ML, Leal JM, Ibeas S (2000) J Org Chem 65:405–410
66. Murray JS, Politzer P (2010) Wiley Interdisciplinary Reviews. Comput Mol Sci 1:153–163
67. Jiao H, PvR S (1994) J Chem Soc Faraday Trans 90:1559–1567
68. White JC, Hess CA (1993) J Phys Chem 97:6398–6404
69. Varetto U < MOLEKEL Version>; Swiss National Supercomputing Centre: Manno (Switzerland), http://wwwbioinformaticsorg/molekel/wiki/Main/HomePage
70. Blake NP, Weakliem PC, Metiu H (1998) J Phys Chem 102:67–74
71. Igarashi K, Tajiri K, Tanemura S, Nanbu R, Fukunaga T (1997) Z Phys D At Mol Clusters 40:562–565
72. Wozniak K, He H, Klinowski J, Jones W, Grech E (1994) J Phys Chem 98:13755–13765
73. Yang Q, Zhong C, Chen JF (2008) J Phys Chem C 112:1562–1569
74. Hafizovic J, Bjørgen M, Olsbye U, Dietzel PDC, Bordiga S, Prestipino C, Lamberti C, Lillerud KP (2007) J Am Chem Soc 129:3612–3620
75. Greathouse JA, Allendorf MD (2006) J Am Chem Soc 128:10678–10679
76. Novakovic SB, Bogdanovic GA, Fraisse B, Ghermani NE, Bouhmaida N (2007) Spasojevic-de Bire A. J Phys Chem A 111:13492–13505